This is a non-peer reviewed preprint submitted to EarthArXiv. This preprint has been submitted to *Earth and Space Science* for peer review.

Horizontal Wavenumber Spectra of Vertical Vorticity and Horizontal Divergence in the Mesosphere and Lower Thermosphere Using Multistatic Specular Meteor Radar Observations

Facundo L. Poblet[*1], Jorge L. Chau[†1], J. Federico Conte[‡1], Victor Avsarkisov[§1], Juha Vierinen[¶2], and Harikrishnan Charuvil Asokan[‖1,3]

[1]Leibniz Institute of Atmospheric Physics at the University of Rostock, Kühlungsborn, Germany
[2]Arctic University of Norway, Tromsø, Norway
[3]Laboratoire de Mécanique des Fluides et d'Acoustique, CNRS, École Centrale de Lyon, Université Claude Bernard Lyon 1, INSA de Lyon, Écully, France

May 6, 2022

Abstract

Specular meteor radars (SMRs) have significantly contributed to the understanding of wind dynamics in the mesosphere and lower thermosphere (MLT). We present a method to estimate horizontal correlations of vertical vorticity (Q_{zz}) and horizontal divergence (P) in the MLT, using line-of-sight multistatic SMRs velocities, that consists of three steps. First, we estimate 2D, zonal, and meridional correlation functions of wind fluctuations using the wind field correlation function inversion (WCFI) technique. Then, the WCFI's statistical estimates are converted into longitudinal and transverse components. The conversion relation is obtained by considering the rotation about the vertical direction of two velocity vectors, from an east-north-up system to a meteor-pair-dependent cylindrical

---

[*] poblet@iap-kborn.de
[†] chau@iap-kborn.de
[‡] conte@iap-kborn.de
[§] avsarkisov@iap-kborn.de
[¶] jvierine@gmail.com
[‖] hari@iap-kborn.de

system. Finally, following a procedure previously applied in the upper troposphere and lower stratosphere to airborne wind measurements, the longitudinal and transverse spatial correlations are fitted, from which Q_{zz}, P, and their spectra are directly estimated. The method is applied to a special SIMONe (Spread Spectrum Interferometric Multistatic meteor radar Observing Network) data set, obtained over northern Germany for seven days in November 2018. The results show that in a quasi-axisymmetric scenario, P was more than five times larger than Q_{zz}, indicating a predominance of internal gravity waves over vertical modes of motion as a possible explanation for the MLT mesoscale dynamics during this campaign.

1 Introduction

The terrestrial atmosphere between tropospheric and mesospheric altitudes contains a diversity of fluid motions, that range from large periods (up to around 30 days), large horizontal extent (thousands of kilometers), namely planetary waves [Rossby, 1939, McCormack et al., 2014], to small-to-medium scale oscillations like gravity waves (GWs) [Hines, 1988] or stratified turbulence regimes [Billant and Chomaz, 2001, Lindborg, 2006]. A typical way to discern the intrinsic nature of the motion is to separate the horizontal velocity wind vectors into a rotational and a divergent component using the Helmholtz decomposition [Lindborg, 2014]. The comparison between the two components, or different estimates associated with them, allows us to build a notion of how the fluid propagates and determines the dominant physical processes.

For example, at synoptic and planetary scales (>1000 km) in the lower atmosphere, the rotational component is dominant. From general circulation models, it was found that its energy content, is about 100 times larger than the energy content of the divergent component [**?**]e.g.¿Augier2013. For smaller horizontal scales, in the tens to hundreds of kilometers (mesoscales), the relative importance is not clear. Many simulations, as well as observational studies, have been carried out in the upper troposphere and lower stratosphere (UTLS) with dissimilar results [Callies et al., 2016, Hamilton et al., 2008]. Hamilton et al. [2008] estimated that the rotational component was more than three times larger than the divergent component near the troposphere. In addition, Skamarock et al. [2014] found the same order of magnitude for the two components in the 8.5-10.5 km tropospheric altitude range and a clearly dominant divergent component (five times larger than the rotational component) in the 16-18 km altitude range.

Observationally, Lindborg [2007] presented a method to quantify the information of the two vector components given by the Helmholtz decomposition. It consists in calculating the vertical component of the two-point correlation tensor of vorticity and the two-point correlation of horizontal divergence. To estimate these functions, the author used one-dimensional longitudinal and transverse structure function components, calculated from velocity measurements in the UTLS, using the MOZAIC (Measurement of Ozone and Water Vapor by Airbus In-Service Aircraft) database of commercial flight measurements [Marenco et al., 1998]. The results showed that the two functions and their spectra had similar orders of magnitude, for horizontal scales up to a couple of hundred kilometers.

Performing such analysis from observations at mesosphere and lower thermosphere (MLT) altitudes poses the difficulty that to obtain correlation or structure functions for displacements of at least several hundreds of kilometers in horizontal directions, the full three-dimensional velocity vector with good horizontal coverage, should be known beforehand, which is not the case. To tackle this problem, Vierinen et al. [2019] introduced the wind field correlation function inversion (WCFI) technique. WCFI uses an indirect way to calculate wind-field correlation functions without previously knowing the complete velocity vectors. The technique has been implemented on lines-of-sight multistatic specular meteor radar velocities to calculate six independent components of the velocity correlation tensor, distributed either in time lags, horizontal or vertical displacements. The method is particularly useful when a dense data set of meteor detections is used.

Monostatic specular meteor radar (SMRs) have been proven to be an essential tool to characterize the mesoscale dynamics in the MLT region. For instance, wind estimates over horizontal areas of a couple of hundred kilometers radius, resolutions of several hours and of 1-2 km in the vertical direction, which are typically well resolved by SMRs [Hocking et al., 2001, Holdsworth et al., 2004], have contributed to the understanding of the climatological behavior of mean winds, planetary waves, and tides [Sandford et al., 2006, Clemesha et al., 2009, Hoffmann et al., 2010]. Besides, SMR measurements have been used to study GW-driven momentum fluxes [Placke et al., 2011, Nicolls et al., 2012, Andrioli et al., 2015, Conte et al., 2021]. In recent years, multistatic SMR configurations have been implemented [**?**]e.g.¿Stober2015,Chau2017,Stober2018,Chau2021, allowing a significant increase in scattering detections per unit time, observing the same volume from different viewing angles.

This work introduces a novel approach for calculating longitudinal and transverse horizontal correlation functions in the MLT. With them, and the formalism developed by Lindborg [2007], the relative importance of internal GWs and vortical modes of motion to explain MLT mesoscale variations can be established. So far, the role of vorticity has been poorly quantified in the MLT mesoscales. Since GW breaking is a primary source of vorticity, it cannot be insignificant. Also, many different mechanisms of coupling between atmospheric regions, like spontaneous imbalances or secondary gravity waves require non-zero vorticity. This study aims to fill this gap in observations by introducing a method to quantify it, in terms of its spatial correlation.

The technique is demonstrated with Spread Spectrum Interferometric Multistatic meteor radar Observing Network (SIMONe) 2018, which was conducted over Northern Germany in November of 2018. SIMONe 2018 led to the detailed characterization of different aspects of the mesospheric wind field, documented in several publications so far [Vierinen et al., 2019, Charuvil Asokan et al., 2022, Vargas et al., 2021, Volz et al., 2021].

This article is organized as follows. Section 2 briefly describes the derivation of the two-point correlation of vertical vorticity and horizontal divergence as was originally done by Lindborg [2007], and their relation to the longitudinal and transverse correlation functions. Section 3 describes the data set and the methodology to obtain the correlation estimates. Section 4 presents the results on the 2D correlation functions, the functional fits used to represent the trends, and the calculation of Lindborg's functions. Section 5 discusses the main points, and Section 6 presents the scope of this work and treats the possible extension of the technique to other applications.

2 Two-point correlation of vertical vorticity (Q_{zz}) and horizontal divergence (P) - Definitions

The Reynolds decomposition of the mesospheric wind field ($\mathbf{u}$)

$$\mathbf{u} = \mathbf{U} + \mathbf{u}' \tag{1}$$

into its mean wind $\mathbf{U} = \langle \mathbf{u} \rangle$ and fluctuating wind $\mathbf{u}'$ part is frequently used to study the wind in different spatio-temporal scales. From equation 1, one would expect that $\langle \mathbf{u}' \rangle = 0$, where $\langle \cdots \rangle$ denotes an ensemble average or expected value. In practice, due to the presence of intermittency, the separation into the mean and fluctuating parts is always strongly dependent on the averaging procedure, and so the mean wind represents different dynamics when it is averaged over one month, 24 hr or 30 min, for example.

The fluctuations $\mathbf{u}'$ can be used to define the two-point correlation tensor of the wind velocity fluctuations R'_{ij}, that for points separated by $\mathbf{s}$ and determined at position $\mathbf{r}$ is

$$R'_{ij}(\mathbf{r}, \mathbf{s}) = \langle u'_i(\mathbf{r}) u'_j(\mathbf{r} + \mathbf{s}) \rangle.$$

The analogous expression for the vorticity vector $\boldsymbol{\zeta} = \nabla_{\mathbf{r}} \times \mathbf{u}'$ is

$$Q_{ij}(\mathbf{r}, \mathbf{s}) = \langle \zeta_i(\mathbf{r}) \zeta_j(\mathbf{r} + \mathbf{s}) \rangle, \tag{2}$$

where Q_{ij} is the two-point correlation tensor of the vorticity. If the velocity field is considered homogeneous in horizontal planes, then for an altitude r_3 we have $R'_{ij} = R'_{ij}(r_3, \mathbf{s})$ and $Q_{ij} = Q_{ij}(r_3, \mathbf{s})$.

The relation between R'_{ij} and Q_{ij} can be derived by inserting in equation 2 the $\boldsymbol{\zeta}$ components ζ_i as a function of u'_i and applying the derivative definition assuming homogeneity. Batchelor [1953, pp. 38 Eq. 3.2.1] gives an elegant solution, that for the vertical component of Q_{ij}, i.e., Q_{33}, hereinafter referred to as Q_{zz}, is

$$Q_{zz} = -\varepsilon_{3ik} \varepsilon_{3jl} \frac{\partial^2 R'_{kl}}{\partial \mathrm{s}_i \partial \mathrm{s}_j}, \tag{3}$$

with summation over repeated indices. ε_{ijk} is the Levi-Civita tensor that accounts for the permutations. Lindborg [2007] expanded equation 3 into a local cylindrical coordinate system (s_h, ϕ, s_z) in which s_h and s_z are the horizontal and vertical distances between two points, and ϕ is the angle between the direction of s_h and a predefined horizontal direction. He found that for a fixed altitude

$$Q_{zz}(s_h) = \frac{1}{s_h}\frac{\partial R'_{s_h s_h}}{\partial s_h} - \frac{1}{s_h^2}\frac{\partial}{\partial s_h}\left(s_h^2 \frac{\partial R'_{\phi\phi}}{\partial s_h}\right). \tag{4}$$

A similar expression can be found using a cartesian coordinate system, as it is presented in A. An important hypothesis assumed to derive equation 4 is axisymmetry, that is when all statistical quantities are invariant under rotations of $\mathbf{s}$ and so derivatives with respect to ϕ vanish.

Similarly, the divergence $\nabla_h \cdot \mathbf{u}'_h$ can be used to define the two-point correlation function of horizontal divergence P [Lindborg, 2007] as

$$P = \langle (\nabla_h \cdot \mathbf{u}'_h(\mathbf{r}))\,(\nabla_h \cdot \mathbf{u}'_h(\mathbf{r}+\mathbf{s}))\rangle = -\frac{\partial^2 R'_{ij}}{\partial \mathrm{s}_i \partial \mathrm{s}_j}. \tag{5}$$

In this case, h stands for horizontal components so the repeated indices in the right-hand side term are summed over the two horizontal orthogonal directions. Expanding the expression, under the assumptions of homogeneity and axisymmetry it is found that

$$P(s_h, s_z) = \frac{1}{s_h}\frac{\partial R'_{\phi\phi}}{\partial s_h} - \frac{1}{s_h^2}\frac{\partial}{\partial s_h}\left(s_h^2 \frac{\partial R'_{s_h s_h}}{\partial s_h}\right). \tag{6}$$

Q_{zz} and P can be directly solved when $R'_{s_h s_h}$ and $R'_{\phi\phi}$ are known. These two components are usually termed as longitudinal $R'_{s_h s_h} = R'_{LL}$ and transverse $R'_{\phi\phi} = R'_{TT}$ components [King et al., 2015a,b]; and so this designation will be maintained along this study.

3 Data set and methods

3.1 SIMONe 2018 campaign

The SIMONe 2018 campaign was conducted in northern Germany for seven consecutive days between November 2 and November 9. It collected approximately one million specular meteor detections over an area of about 500×500 km in the MLT region. This extraordinary number of observations was the synthesis of several new techniques, designed in recent years to increase the number of measurements. Firstly, the multistatic, multi-frequency Agile Radar for Investigations of the Atmosphere (MMARIA) concept was used, which is a multistatic and multi-frequency approach for SMRs to improve MLT wind determinations [Stober and Chau, 2015]. Secondly, a new coded multiple-input–multiple-output, continuous-wave transmitter was used [Vierinen et al., 2016, Chau et al., 2019]. Thirdly, the interferometry and compressed sensing were made with multiple transmitters and receivers following Urco et al. [2018, 2019]. The measurements consist of Bragg vectors and Doppler frequencies with their corresponding statistical uncertainties.

The radar network consisted of two pulsed transmitters in Collm (51.31° N, 13.00° E) and Juliusruh (54.63° N, 13.37° E), operating at 36.2 MHz and 32.55 MHz, respectively; and one coded–continuous-wave transmitter located in Kühlungsborn (54.15° N, 11.76° E), that consisted of five antennas that transmitted different pseudo-random binary phase code. The antennas were deployed in a pentagon configuration, which presents some benefits compared to the Jones configuration, typically used in monostatic SMRs [Espy et al., 2004]. For instance, the signal presents sidelobes with larger separation, lower amplitude, and better symmetry [Younger and Reid, 2017, Chau and Clahsen, 2019]. Figure 1 shows a map of the region where the campaign took place. The transmitters are placed as green triangles.

The transmitter locations were also receiving sites. In addition, there were six other places with receivers only, that are depicted as white dots in Figure 1. The reception mode and reception type for each place is specified in Charuvil Asokan et al. [2022, Table 1].

Figure 1 also shows a 2D histogram for the total number of specular meteor observations detected during the campaign as red, orange and yellow tones in logarithmic scale. The color bar values are the number of detections within bins of 0.1° wide in Latitude and Longitude. The horizontal distribution of meteors was almost uniform in all directions. This is important to calculate reliable correlation values in multiple horizontal directions, as it is explained in Section 3.3. Also, the vertical distribution presented maxima in the $\sim$87-96 km range [Charuvil Asokan et al., 2022, see Figure 1b], that lies in the mesopause region [Xu et al., 2007], below the Kármán line at the edge of outer space [McDowell, 2018].

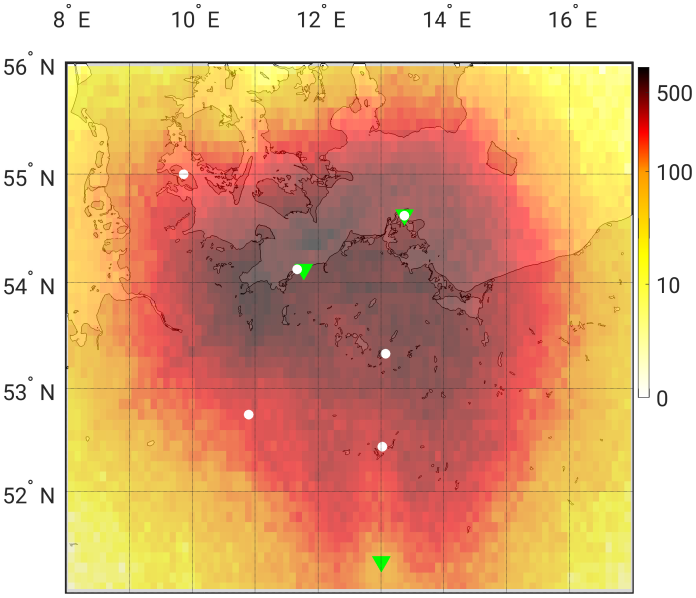

Figure 1: Transmitting and receiving sites during the Spread Spectrum Interferometric Multistatic meteor radar Observing Network (SIMONe) 2018 campaign. The green triangles mark the location of the transmitters and the white circles mark the location with receivers only. The red, orange and yellow tones represent a 2D histogram for the total number of specular meteor observations detected during the campaign. The color bar values show the number of detections within bins of 0.1° wide in Latitude and Longitude.

3.2 Mean wind velocity estimations in time and altitude

A direct consequence of the meteor trails drifting with the mesospheric neutral wind, is that their Doppler shifts (f) can be expressed as

$$2\pi f = \mathbf{u} \cdot \mathbf{k} + \xi \tag{7}$$

where $\mathbf{u} = (u_1, u_2, u_3) = (u, v, w)$ is the full wind vector as defined in equation 1 in the local meteor-centered east-north-up (ENU) cartesian coordinate system, with u, v and w referring to the zonal (east-west), meridional (north-south) and vertical (up-down) components, respectively. The Bragg wave vector $\mathbf{k} = (k_u, k_v, k_w)$ is obtained from the subtraction between the scattered and incident vector, and ξ is the error [Hocking et al., 2001, Holdsworth et al., 2004].

Equation 7 is classically solved for $\mathbf{u}$ in time and altitude bins using least-squares methods. Then, for every time-altitude bin, the wind estimations are representative of a large horizontal area, where the maximum limit is constrained by the total horizontal range covered by the data. This means that the solutions are mean winds $\mathbf{U}$, and depending on the resolutions that are selected to calculate them, they represent average characteristics of different processes.

In the case of monostatic SMRs, the mean wind is frequently calculated in hourly values every 2-3 km of altitude [Jacobi et al., 1999, Hoffmann et al., 2010]. For multistatic SMR networks, the resolutions can be considerably improved due to the larger amount of meteor detections. Time and vertical resolution values can be of $\sim$15 min and 1 km, respectively [Stober and Chau, 2015, Conte et al., 2021]. In this case, as multistatic SMRs observe the same mesospheric volume from different viewing angles, horizontal gradients that contain vorticity information can be determined [Chau et al., 2017, Zhong et al., 2021].

Examples of mean winds estimated with different time and altitude resolutions can be seen in Conte et al. [2021, Figure 4] for measurements carried out in southern Patagonia, or in Chau et al. [2017, Figure 4] using SMRs located in Tromsø, Norway. The winds are estimated by the linear least-square method and show the typical behavior of winds at mesospheric altitudes i.e. strong velocity changes from positive to negative throughout a day or a couple of days. Tidal modes can also be recognized.

For the SIMONe 2018 campaign, the mean winds are presented by Charuvil Asokan et al. [2022, Figure 2] and Vargas et al. [2021, Figure 2], estimated using 30 min and 1 km bins. The semidiurnal tide was dominant in both horizontal components and indications of higher-frequency fluctuations, in the order of hours can be recognized. These fluctuations are better observed if mean winds calculated with larger temporal and vertical resolutions are subtracted. The residuals winds that result from subtracting the 4 hr, 4 km resolution winds, presented coherent gravity wave features in both horizontal components. In general, removing the 4 hr, 4 km mean winds works well to study fluctuating winds that include gravity waves activity [Conte et al., 2021].

3.3 Wind field correlation function inversion to calculate 2D horizontal correlation functions

The essence of the WCFI method is in considering products of Doppler shifts of meteor detections that occur in a different time and location to estimate correlation functions. Given two detections n and m at times t_n, t_m and positions $\mathbf{r}_n$, $\mathbf{r}_m$; with their corresponding velocities $\mathbf{u}_n$, $\mathbf{u}_m$; Doppler shifts f_n, f_m; Bragg wave vectors $\mathbf{k}_n$, $\mathbf{k}_m$; and errors ξ_n, ξ_m; for their Doppler shifts (equation 7) product we have:

$$4\pi^2 f_n f_m = (\mathbf{u}_n \cdot \mathbf{k}_n)(\mathbf{u}_m \cdot \mathbf{k}_m) + (\mathbf{u}_n \cdot \mathbf{k}_n)\,\xi_m + (\mathbf{u}_m \cdot \mathbf{k}_m)\,\xi_n + \xi_n \xi_m. \qquad (8)$$

If the expected or mean value of equation 8 is calculated, considering a sufficient amount of meteors n and m, only the first term on the right-hand side is different than zero. This is because the errors are assumed to be zero-mean, independent, and normally distributed random variables and the mesospheric winds can usually be modeled as a stationary and horizontally homogeneous stochastic process. The resulting expression has the form

$$\langle 4\pi^2 f_n f_m \rangle = \langle (\mathbf{u}_n \cdot \mathbf{k}_n)\,(\mathbf{u}_m \cdot \mathbf{k}_m) \rangle. \tag{9}$$

Vierinen et al. [2019] showed that if equation 9 is expanded in terms of the vectors components, a linear system can be formed as

$$\mathbf{y} = \mathbf{A}\tilde{\mathbf{x}} + \boldsymbol{\eta}, \tag{10}$$

in which $\mathbf{y}$ is an array of values containing the cross product between the Doppler shifts of different meteors, $\mathbf{A}$ is a matrix containing products and summations that involve the Bragg vector components of the different meteor detections, $\tilde{\mathbf{x}}$ is the least-square solution of the system that gives the correlation tensor components distributed in temporal and spatial lags, and $\boldsymbol{\eta}$ are the associated errors on solving the system. The reader can examine the detailed form of the matrix $\mathbf{A}$ in Vierinen et al. [2019, equation 14].

More specifically, the solution $\tilde{\mathbf{x}}$ is given by the array

$$\tilde{\mathbf{x}} = [R_{uu}(\tau, \mathbf{s})\; R_{vv}(\tau, \mathbf{s})\; R_{ww}(\tau, \mathbf{s})\; R_{uv}(\tau, \mathbf{s})\; R_{uw}(\tau, \mathbf{s})\; R_{vw}(\tau, \mathbf{s})]^{\intercal}, \tag{11}$$

where $R_{ij}(\tau, \mathbf{s}) = \langle u_i(t_n, \mathbf{r}_n) u_j(t_m, \mathbf{r}_m) \rangle$ are the six unique components that are retrieved by the method. $R_{ij}(\tau, \mathbf{s})$ depend on temporal and spatial displacements (also called lags) $\tau = t_m - t_n$ and $\mathbf{s} = \mathbf{r}_m - \mathbf{r}_n$. The criterion implemented to combine the meteors to solve the system gives the nature of the correlations, because it determines the ranges of τ or $\mathbf{s}$, resulting in temporal or spatial correlations.

The meteors are combined in pairs. For spatial, horizontal correlations distributed in two dimensions, i.e., east-west (x) and north-south (y) directions, the meteor pairs are formed in the following manner. Since SMRs detect meteors continuously in time, approximately between 70 and 110 km of altitude, the first step is to confine these ranges. Then, the data in an interval of 6 or 2 km wide, and one day or one week are selected.

After that, the pairing scheme moves to particular detections. We select one meteor n and tune the vertical and temporal conditions, finding every meteor that is not separated from it by more than a given temporal and vertical resolution ($\Delta\tau$ and Δs_z, respectively). Then, for each meteor fulfilling the temporal and vertical requirements, only those meteors that lie in the intervals $\mathbf{s} \pm \Delta\mathbf{s}/2 = (\mathrm{s}_x \pm \Delta\mathrm{s}_x/2, \mathrm{s}_y \pm \Delta\mathrm{s}_y/2)$ for particular values of $\mathbf{s} = (\mathrm{s}_x, \mathrm{s}_y)$ and fixed horizontal lag resolutions $\Delta\mathrm{s}_x = \Delta\mathrm{s}_y$, are selected. The meteor pairs are formed by combining the meteor n with each one of the resulting meteors.

The procedure continues by selecting another meteor to play the role of n in the previous step, and repeat the process. In the end, every pair has in common that their elements preserve the distance between each other (within the horizontal resolution ranges).

Finally, with every non-repeated meteor pair, the system in equation 10 is solved for the correlation components $R_{ij}(\mathrm{s}_x, \mathrm{s}_y)$.

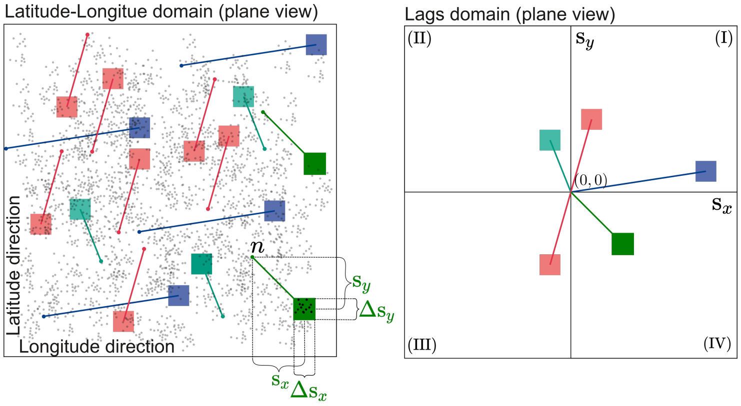

Figure 2: Schematic representation of the meteors selection procedure to calculate 2D correlation functions. Left panel: plane view showing different geometries to form the meteor pairs. The gray dots represent meteor positions mapped into a plane in Latitude and Longitude for the given altitude range. The colors represent different geometries, given by the values of s_x and s_y. Right panel: Position in the lags domain where the correlations are calculated. The colors represent different values of s_x and s_y.

Figure 2 helps to schematically visualize the transition from the Latitude-Longitude domain, i.e., where the measurements are taken, to the spatial horizontal lags domain, i.e., where the correlation functions are calculated. The gray dots in the left-hand side panel represent the meteor positions mapped into a plane in Latitude and Longitude for the given altitude range. The colors represent different geometries, that manifest in the values of s_x and s_y, because the resolutions $\Delta\mathrm{s}_x$ and $\Delta\mathrm{s}_y$ are kept constant. The straight lines mark the distance between the starting point and the center of the searching area, of dimension $\Delta\mathrm{s}_x\Delta\mathrm{s}_y$. If we look at the meteor n, the pairs are formed with the meteors that lie inside the green box, after the temporal and vertical filtering. For this particular geometry, the total amount of pairs is obtained when the process is extended to every meteor, considering the same s_x and s_y (every geometry in green for all the meteors). With every pair, the correlations are mapped to the corresponding $\mathbf{s}$ value, sketched also in green color on the right-hand side panel of the figure. In particular, note that for the sketches in red, that show opposite geometries, the relation $R_{ij}(\mathbf{s}) = R_{ij}(-\mathbf{s})$ is valid, because almost the same measurements are used to form the pairs for both cases. Consequently, the method produces only two quadrants with independent correlations to analyze: (I) and (II), (I) and (IV), (II) and (III) or (III) and (IV).

3.3.1 Fluctuating wind correlations

In Section 3.3, the WCFI method was introduced for the more general case, that is when the correlations of the total wind R_{ij} are needed. To estimate the two-dimensional correlations of the fluctuating wind R'_{ij}, two approaches can be followed. The first one is to calculate the full correlation tensor in which correlations in short and long lags can be identified and also calculate another correlation tensor with lower resolutions over a large temporal and spatial extent. The difference between both gives the correlation functions of the fluctuating wind. In general, short lags show the contribution of the fluctuating winds while long lags capture the contributions of the mean winds.

The second method consists of filtering the Doppler shifts before applying the WCFI method. This is achieved by estimating $\mathbf{U}$, using the procedure introduced in Section 3.2. In particular, solving equation 7 with low resolutions, for example 4 hr, 4 km; so the filtered Doppler shifts f' are $f' = f - \mathbf{U} \cdot \mathbf{k}/2\pi$ with f' the Doppler shift measurement of the high-pass-filtered wind. Then, the WCFI technique is applied using f' and $\mathbf{k}$ to get 2D correlation functions of the fluctuating wind. As stated by Vierinen et al. [2019], high-pass-filtered measurements have shorter temporal and spatial lengths, resulting in more independent samples of the wind field correlation function to be obtained per unit of time and space. The second approach was followed in this work. We subtracted mean winds calculated every 1 km and 30 min; with resolutions of 4 hr and 4 km.

3.4 Transformation from zonal-meridional (R_{uu}, R_{vv}) to longitudinal-transverse components (R_{LL}, R_{TT})

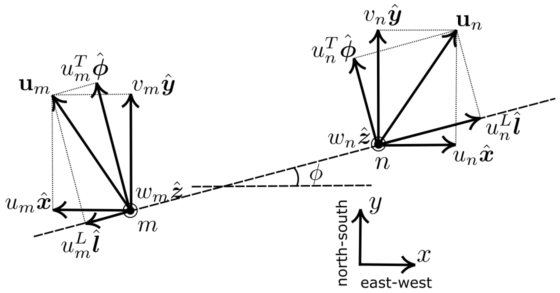

Figure 3: Schematic diagram showing the wind velocity vectors for two different detections n and m on a plane view. The vectors are decomposed in longitudinal, transverse and vertical components u^L, u^T and w and in Cartesian ENU components u, v and w. $\hat{\boldsymbol{l}}$, $\hat{\boldsymbol{\phi}}$, $\hat{\boldsymbol{z}}$ and $\hat{\boldsymbol{x}}$, $\hat{\boldsymbol{y}}$, $\hat{\boldsymbol{z}}$ are the unit vectors of the two systems.

The WCFI method delivers 2D horizontal correlation functions in cartesian ENU components. These components are given by the solution array in equation 11. In order to use the WCFI method solutions to solve equations 4 and 6 we must find a way to convert R_{uu} and R_{vv} to R_{LL} and R_{TT}. This can be done using a post-statistic approach under certain conditions. The conversion method is described in this section.

Similarly to section 3.3, we consider the two points n and m that represent two meteor detections depicted in the diagram of Figure 3. At these two points, the neutral wind velocities are $\mathbf{u}_n$ and $\mathbf{u}_m$. These vectors can be decomposed in longitudinal, transverse and vertical components $\mathbf{u}_n = u_n^L\hat{\boldsymbol{l}} + u_n^T\hat{\boldsymbol{\phi}} + w_n\hat{\boldsymbol{z}}$, $\mathbf{u}_m = u_m^L\hat{\boldsymbol{l}} + u_m^T\hat{\boldsymbol{\phi}} + w_m\hat{\boldsymbol{z}}$, where we have used the local, meteor-pair dependent basis $\hat{\boldsymbol{l}}$, $\hat{\boldsymbol{\phi}}$, $\hat{\boldsymbol{z}}$, with $\hat{\boldsymbol{z}}$ in the vertical direction, $\hat{\boldsymbol{l}}$ perpendicular to $\hat{\boldsymbol{z}}$ along the line that connects both meteors and $\hat{\boldsymbol{\phi}}$ perpendicular to $\hat{\boldsymbol{l}}$ and $\hat{\boldsymbol{z}}$. The figure also shows the decomposition in the ENU system $\mathbf{u}_n = u_n\hat{\boldsymbol{x}} + v_n\hat{\boldsymbol{y}} + w_n\hat{\boldsymbol{z}}$, $\mathbf{u}_m = u_m\hat{\boldsymbol{x}} + v_m\hat{\boldsymbol{y}} + w_m\hat{\boldsymbol{z}}$, where the basis $\hat{\boldsymbol{x}}$, $\hat{\boldsymbol{y}}$, $\hat{\boldsymbol{z}}$ are on the east-west ($\hat{\boldsymbol{x}}$), north-south ($\hat{\boldsymbol{y}}$) and vertical ($\hat{\boldsymbol{z}}$) directions. In the case of the vertical components, they are the same for both systems. On the other hand, the horizontal components in the two systems are related by a rotation of an angle (ϕ) around the vertical axis. The relation, for the point n for example, is

$$u_n^L = u_n \cos\phi + v_n \sin\phi, \tag{12}$$

$$u_n^T = -u_n \sin\phi + v_n \cos\phi, \tag{13}$$

deduced considering the well-known conversion of a velocity vector from Cartesian to Cylindrical components, or by using geometrical arguments in Figure 4.

We can extend equation 12 for point m, and build R_{LL} as

$$\begin{aligned} R_{LL}(\mathbf{s}) &= \langle u_n^L(\mathbf{r}_n)u_m^L(\mathbf{r}_m)\rangle \\ &= \langle u_n(\mathbf{r}_n)u_m(\mathbf{r}_m)\cos^2\phi\rangle + \langle u_n(\mathbf{r}_n)v_m(\mathbf{r}_m)\cos\phi\sin\phi\rangle \\ &+ \langle u_m(\mathbf{r}_m)v_n(\mathbf{r}_n)\sin\phi\cos\phi\rangle + \langle v_n(\mathbf{r}_n)v_m(\mathbf{r}_m)\sin^2\phi\rangle, \end{aligned} \tag{14}$$

in which ideally, when the velocity vectors in ENU components are fully known, the expected values of the four terms are calculated combining the products of the sines, cosines and velocity components of every detection. In our case, this scenario is not feasible since we do not know the velocity vectors of every detection. However, once the correlation tensor components are calculated with the WCFI method, we can assume that for every detection within $\mathbf{s} \pm \Delta\mathbf{s}/2$, ϕ is approximately constant. Then, the ϕ-dependent products of equation 14 can be taken out the expected value operator to get the following expression

$$R_{LL}(\mathbf{s}) \simeq R_{uu}(\mathbf{s})\cos^2\phi + 2R_{uv}(\mathbf{s})\cos\phi\sin\phi + R_{vv}(\mathbf{s})\sin^2\phi, \tag{15}$$

that considering horizontal isotropy ($R_{uv} = R_{vu} = 0$) becomes

$$R_{LL}(\mathbf{s}) \simeq R_{uu}(\mathbf{s})\cos^2\phi + R_{vv}(\mathbf{s})\sin^2\phi. \tag{16}$$

It is very important for equations 15 and 16 to be valid that $|\Delta\mathbf{s}| < |\mathbf{s}|$, otherwise ϕ cannot be considered as a constant value for the given $\mathbf{s}$. Therefore, if the resolution is fixed, equations 15 and 16 are not valid for small lags.

Repeating the same procedure for R_{TT}, similar expressions are obtained

$$R_{TT}(\mathbf{s}) \simeq R_{uu}(\mathbf{s})\sin^2\phi - 2R_{uv}(\mathbf{s})\cos\phi\sin\phi + R_{vv}(\mathbf{s})\cos^2\phi, \tag{17}$$

and

$$R_{TT}(\mathbf{s}) \simeq R_{uu}(\mathbf{s}) \sin^2\phi + R_{vv}(\mathbf{s}) \cos^2\phi, \tag{18}$$

for the isotropic case.

4 Results

4.1 2D horizontal correlation functions

The 2D correlation function components $R'_{uu}(\mathbf{s})$, $R'_{vv}(\mathbf{s})$ and $R'_{uv}(\mathbf{s})$ calculated for the SIMONe 2018 campaign can be seen in panels (a), (b) and (c) of Figure 4, respectively. The white lines are smoothed contours of the correlations, plotted to visualize the behavior for different directions. Also, the correlation errors are shown as light-blue contours in the three panels.

$R'_{uu}(\mathbf{s})$, $R'_{vv}(\mathbf{s})$ and $R'_{uv}(\mathbf{s})$ were estimated using detections within the 87-93 km altitude range, and considering time and altitude resolutions of $\Delta\tau = 30$ min and $\Delta s_z = 1$ km, respectively; and horizontal resolutions of $\Delta \mathrm{s}_x = \Delta \mathrm{s}_y = 25$ km. We calculated the correlations every 12.5 km in both directions, s_x and s_x, covering the displacements range given by $\mathrm{s}_x = [-250, 250]$ km and $\mathrm{s}_y = [0, 400]$ km; i.e., only the quadrants I and II were considered to avoid working with repeated information (see the pairs selection procedure described in section 3.3). The white areas for large $|\mathbf{s}|$ values mark correlations with errors larger than 25 m^2 s^{-2}, that were excluded from the analysis.

R'_{uu} and R'_{vv} show a gradual decorrelation as $|\mathbf{s}|$ increases, and R'_{uv} presents comparatively lower values of correlations in the entire domain. The decrease of R'_{uu} and R'_{vv} is not identical in every direction for certain separation ranges. For example, a moderate alignment in the northwest/southeast direction can be identified for both components. This behavior is more clear for mid-range lags, around horizontal lags $s_h = \sqrt{\mathrm{s}_x^2 + \mathrm{s}_y^2} \simeq 150$ km, and disappears for shorter values. For larger lags, the correlations increase their dispersion due to the increase in errors. The cross-correlation component $R'_{uv} \simeq 0$, meaning that the background wind was correctly calculated and there was no preferential direction for the fluctuating wind during the campaign. As a result, u and v variations are approximately uncorrelated. The relatively high correlation values reached by R'_{uv} lie in the longest displacements region, where the errors are the largest as well.

In general, the errors of the three components increase as the lags grow, partially because there are less number of pairs in longer lags to resolve the correlations with high precision. Figure 4(d) shows the gradual decrease in the number of pairs as lag values increase.

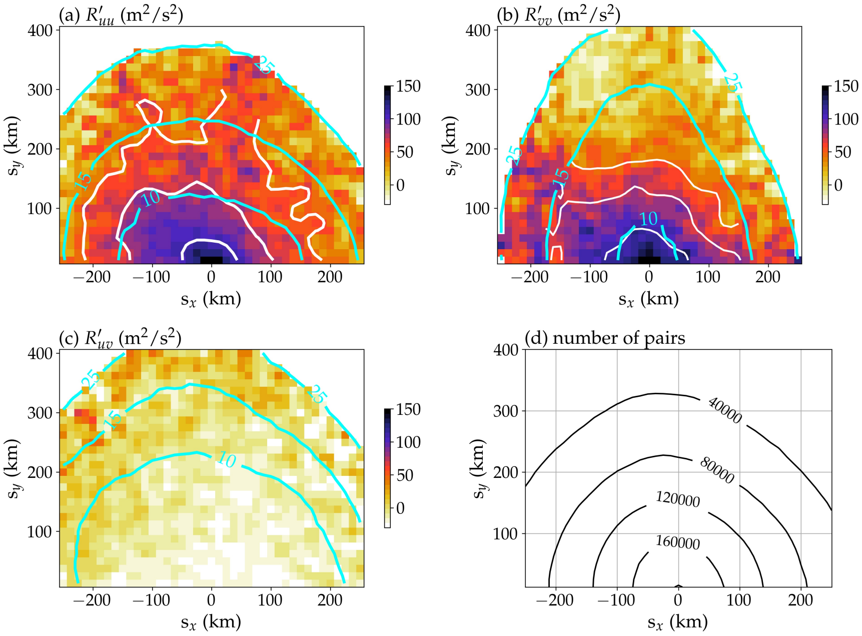

Figure 4: 2D correlation functions and number of meteor pairs during the SIMONe 2018 campaign. Panels (a), (b) and (c) show R'_{uu}, R'_{vv} and R'_{uv} components, respectively. The light-blue lines are the correlation errors in units of $\mathrm{m}^2/\mathrm{s}^2$ and the white lines in panels (a) and (b) are smoothed contours, showing decorrelation patterns along different directions. Panel (d) shows the number of meteor pairs as a function of the horizontal displacements $\mathbf{s} = (\mathrm{s}_x, \mathrm{s}_y)$.

4.2 1D longitudinal and transverse correlation and structure functions

In order to estimate $Q_{zz}(s_h)$ and $P(s_h)$ from equations 4 and 6, $R'_{uu}(\mathbf{s})$ and $R'_{vv}(\mathbf{s})$ in Figure 4 were converted into $R'_{LL}(\mathbf{s})$ and $R'_{TT}(\mathbf{s})$, applying the relations 16 and 18, and then reduced to the radial dependence s_h, setting an exclusion lags region of $|\Delta\mathbf{s}|/|\mathbf{s}| < 0.8$. When applying the dimensional reduction from 2D to 1D, several correlation values are mapped to the same s_h value because it is calculated with fixed steps of s_x and s_y using the relation $s_h = \sqrt{\mathrm{s}_x^2 + \mathrm{s}_y^2}$. Note that this implies that there are less correlation values at initial lags. To work with single correlation values for each lag, we estimated mean correlations for each s_h value.

The results for R'_{LL} and R'_{TT} are presented as black dots in panels (a) and (b) of Figure 5, respectively. The error bars, determined by summation in quadrature, are also added to the plots. Both components present increasing dispersion as the lag values grow. Yet, it can be noted from casually examining the trends that they progressively reduce their values, going to zero at $s_h \simeq 350$ km for R'_{LL} and at longer lags for R'_{TT}, which are out of the measurements ranges.

The physical mechanisms behind correlation functions can be investigated by making use of the second-order structure functions D_{LL} and D_{TT}. In the homogeneous case, both components are linked to the correlation functions by [Frisch, 1995, Kolmogorov, 1941, Schulz-DuBois and Rehberg, 1981]

$$R_{LL}(s_h) = R_{LL}(0) - \frac{1}{2} D_{LL}(s_h), \tag{19}$$

$$R_{TT}(s_h) = R_{TT}(0) - \frac{1}{2} D_{TT}(s_h), \tag{20}$$

where $R_{LL}(0)$ and $R_{TT}(0)$ are the correlations at zero lag. The advantage of using structure functions is that if $D_{LL}(s_h) \propto s_h^{\gamma-1}$ with $1 \leq \gamma \leq 3$, then their spectral shape follows a power law $k^{-\gamma}$ where k is the wavenumber (the same reasoning is valid for D_{TT}). In addition, structure functions are less sensitive to low-frequency oscillations than correlation functions [Schulz-DuBois and Rehberg, 1981]. In terms of structure functions, the well known $\gamma = 5/3$ spectral power law found by Nastrom et al. [1984] for wavelengths $\lesssim 500$ km corresponds to 2/3 and the $\gamma = 3$ for wavelengths around 1000-3000 km, to 2.

Then, considering the s_h ranges that we investigate, R'_{LL} and R'_{TT} can be approximated by the functions

$$\hat{R}'_{LL} = a_0 - a_1 s_h^{2/3} \tag{21}$$

$$\hat{R}'_{TT} = b_0 - b_1 s_h^{2/3}, \tag{22}$$

where a_0 and b_0 are the estimates for the zero-lag correlations and a_1, b_1 the parameters that represent the energy-cascade dynamical origin. We have carried out these fits over the mean values of R'_{LL} and R'_{TT}, and the resulting curves are presented as orange lines in panels (a) and (b) of Figure 5, for R'_{LL} and R'_{TT}, respectively.

$\hat{R}'_{LL}$ and $\hat{R}'_{TT}$ follow the trends of the observed correlations fairly well. We can infer the goodness of the fit, in terms of the root mean square (RMS), with; RMS = 8.61 for R'_{LL} and RMS = 10.75 for R'_{TT}. Although they are in the same order of magnitude, the RMS is a bit larger for R'_{TT}, which can be caused by the fact that at $s_h \lesssim 75$ km and $s_h \simeq 360$ km, the observations depart from the fit predictions.

Using a_0 and b_0, the structure functions can be determined as

$$D'_{LL} = 2\left(a_0 - R'_{LL}\right), \tag{23}$$

$$D'_{TT} = 2\left(b_0 - R'_{TT}\right), \tag{24}$$

and the corresponding fits are $\hat{D}'_{LL} = 2a_1 s_h^{2/3}$ and $\hat{D}'_{TT} = 2b_1 s_h^{2/3}$. On these definitions, we are assuming that the correlations at zero lag are constant, given by $R'_{LL}(0) = a_0$ and $R'_{TT}(0) = b_0$ (homogeneous medium). Since the region containing the shortest lags is excluded when estimating the longitudinal and transverse correlation components (see section 3.4), it is not possible to use a measured zero-lag approximation for $R'_{LL}(0)$ and $R'_{TT}(0)$. D'_{LL} and D'_{TT} are plotted as black crosses in panels (c) and (d) of Figure 5, respectively. The fitting functions are also added to the plots as orange curves.

The agreement of D'_{LL} with a 2/3-power law of s_h is remarkable. This is expected for horizontally distributed second-order structure functions in these scales [Nastrom et al., 1984]. Even though D'_{TT} values have a larger dispersion, the 2/3-power approximation follows the general trends as well.

Other dynamical effects can be considered to fit the observations. Lindborg [1999] proposed functional dependencies for second-order structure functions that incorporate not only an energy cascade mode but an enstrophy-cascade dynamical origin. For this, two terms are incorporated into the fitting models, to capture the variations for large scales, in the $\gamma = 3$ range [Lindborg, 1999, Eq. 68-69]. Since our measurements cover a more narrow range in the mesoscales, the enstrophy-cascade terms were not incorporated to fit the observations.

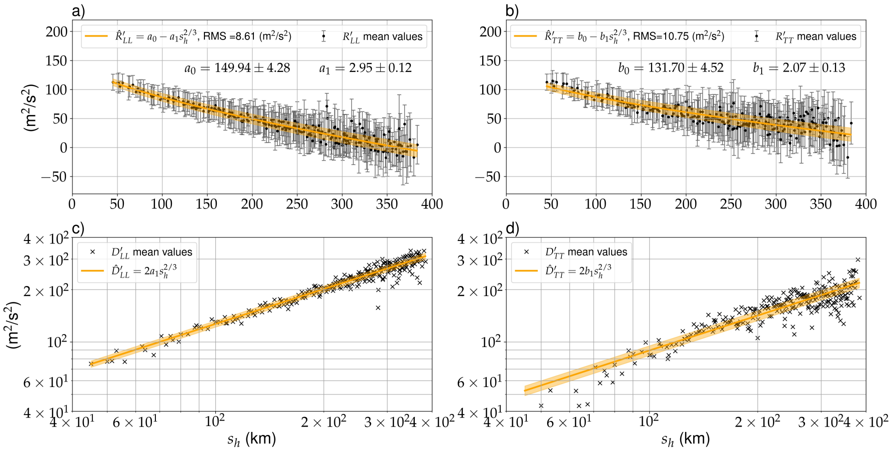

Figure 5: Panels (a) and (b) show the longitudinal and transverse correlation functions (black dots), respectively, as a function of the horizontal lags s_h, during the SIMONe 2018 campaign. The error bars are shown in gray. The orange curves show fits and their uncertainties are presented as shaded areas. Panels (c) and (d) present the second-order longitudinal and transverse structure functions, respectively. The observed values are shown as black crosses and the corresponding fits as orange curves. For clarity purposes, the errors are not shown in these panels.

4.3 Vertical vorticity and horizontal divergence correlations and spectra estimations

Once the parameters of the models proposed to represent R'_{LL} and R'_{TT} are determined, we can make use of equations 4 and 6 to calculate Q_{zz} and P. Introducing equations 21 and 22 into equations 4 and 6 and calculating the derivatives it is found that

$$Q_{zz} = q_1 s_h^{-4/3}, \quad P = p_1 s_h^{-4/3}, \tag{25}$$

with $q_1 = \frac{2}{3}\left(\frac{5}{3}b_1 - a_1\right) = 0.34 \times 10^{-2}\mathrm{m}^{4/3}\mathrm{s}^{-2}$ and $p_1 = \frac{2}{3}\left(\frac{5}{3}a_1 - b_1\right) = 1.90 \times 10^{-2}\mathrm{m}^{4/3}\mathrm{s}^{-2}$. Both functions are plotted in the left-hand side panel of Figure 6 as blue and green lines for Q_{zz} and P, respectively. The black dashed lines indicate the extrapolation to larger and shorter (not measured) displacements.

The characteristics of both functions can be inferred from the parameter values as well as from the plots. For example, it is clear that they quickly go to zero as s_h grows. P reduces its values about a hundred times from the shortest displacement where $P \simeq 0.01$ s^{-2} to the largest displacement where $P \simeq 0.0007$ s^{-2}. On the other hand, $Q_{zz} \lesssim 0.002$ s^{-2} for the entire s_h range. Moreover, with the coefficients q_1 and p_1, we can estimate the ratio $P/Q_{zz} = p_1/q_1 = 5.6$, meaning that P is more than five times larger than Q_{zz}; i.e., a clear predominance of P over Q_{zz}.

The two-dimensional horizontal spectra of Q_{zz} for wavenumbers $k = 2\pi/s_h$ can be calculated as

$$\Phi(k) = 2\pi k \mathcal{F}[Q_{zz}], \tag{26}$$

where the fourier transform, expressed in polar cylindrical coordinates is

$$\mathcal{F}[Q_{zz}] = \frac{1}{4\pi^2}\int_0^{\infty}\int_0^{2\pi} Q_{zz}(s_h)\exp\left(-i\mathbf{s}\cdot\boldsymbol{k}\right)\, s_h \,\mathrm{d}s_h \,\mathrm{d}\phi. \tag{27}$$

If $\boldsymbol{k} = (k, \theta)$, the inner product in the exponential takes the form $\mathbf{s}\cdot\boldsymbol{k} = s_h k\cos(\phi - \theta)$, but since ϕ goes from 0 to 2π, the integral on the angle does not depend of θ. Q_{zz} is only a function of s_h, so we can write Φ as

$$\Phi(k) = k\int_0^{\infty} Q_{zz}(s_h)\; J_0(s_h k) s_h \;\mathrm{d}s_h, \tag{28}$$

in which $J_0(s_h k) = \frac{1}{2\pi}\int_0^{2\pi}\exp\left(-ik\, s_h\cos\phi\right)\mathrm{d}\phi$ is the cylindrical Bessel function of zero order. Replacing Q_{zz} in equation 28, and changing the integration variable $\eta = s_h k$, we get the expression

$$\Phi(k) = q_1 k^{1/3}\int_0^{\infty}\eta^{-1/3} J_0\left(\eta\right)\;\mathrm{d}\eta, \tag{29}$$

in which the integral can be taken from tabulated values to get

$$\Phi(k) \simeq 1.57 q_1 k^{1/3}. \tag{30}$$

An obvious problem to solve equation 29 with this procedure is that Q_{zz} is only known in a bounded s_h interval, that in the wavenumber domain is $k \in [2\pi/383.07, 2\pi/45.07] = [0.016, 0.139]$ km^{-1}. The method is valid if we can assume that the contributions to the spectra outside these limits are small compared to a given k value inside the domain [Lindborg, 2007].

Repeating the exact same procedure for the spectrum of P, hereinafter referred to as Ψ, we get

$$\Psi(k) \simeq 1.57 p_1 k^{1/3}. \tag{31}$$

Φ and Ψ are shown in the right-hand side panel of Figure 6 in the same color code as their corresponding functions in the space domain. The main feature of this plot is that $\Psi > \Phi$ in the entire mesoscales range studied, demonstrating the prevalence of P over Q_{zz} in the wavenumbers domain. Also, $\Psi/\Phi = P/Q_{zz} = 5.6$ showing that the scaling between the two functions is maintained.

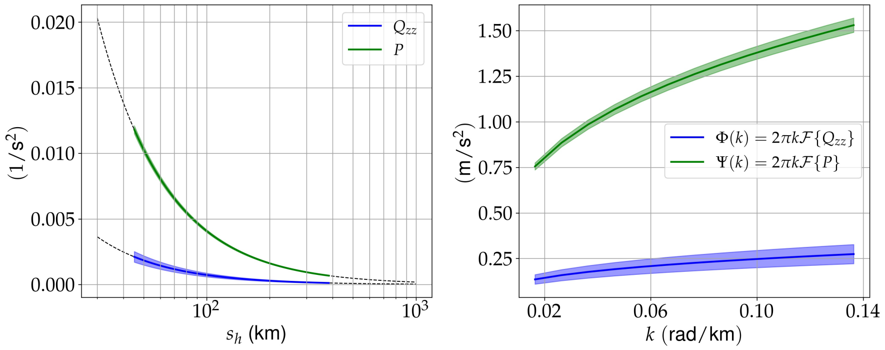

Figure 6: Left panel: Q_{zz} (blue) and P (green) as a function of the spatial lags s_h. The shaded area shows Q_{zz} and P calculated using the uncertainties of the fits in equations 21 and 22. The dashed black lines show the continuation for larger and shorter (not measured) horizontal lags. Right panel: Q_{zz} and P spectra (Φ and Ψ, respectively) as a function of the wavenumber $k = 2\pi/s_h$. The same color coding as for Q_{zz} and P is used.

5 Discussion

Longitudinal and transverse horizontal correlation functions of wind fluctuations in the MLT have been determined by making use of the WCFI technique. These functions were further analyzed to study the vorticity-tensor vertical component and horizontal divergence correlation functions. The detection range enabled the examination of horizontal displacements in the mesoscales, from about 40 to 400 km, in which the vorticity and divergence estimates account for different physical phenomena. On the one hand, Q_{zz} may represent pancake-like structures with fine vertical resolutions in ∼300 m - 1 km [Avsarkisov et al., 2022]. Eddies in strongly stratified fluids can spread in horizontal planes, forming such structures with non-zero vertical vorticity. On the other hand, the divergent component given by P is composed of motions that are not hydrostatically and geostrophically balanced, such as GWs or stratified turbulence, which are the probable physical processes behind P.

It is found that P spectrum was more than five times larger than the Q_{zz} spectrum during the campaign. This result can be compared with the ones obtained by Lindborg [2007], in which the same orders of magnitude for both spectra were observed, with the vorticity spectrum a bit larger than the divergence spectrum. From this, the author argued that the mesoscale energy spectrum could not be generated by internal GWs, otherwise the divergence spectrum would have dominated over the vorticity spectrum. We can extend this reasoning to the results of our study to speculate that for MLT altitudes, internal GWs may be more important than vortical modes to explain the wind dynamics.

However, one must be cautious with the generalization of this assertion because we are using a much more limited data set than the one used by Lindborg [2007], and so the relative predominance of the divergent component might be representative of the campaign time conditions. In fact, according to the recent work by Vargas et al. [2021], the campaign presented a significant activity of small- and large-scale GWs interacting with the mean wind flow. In particular, Charuvil Asokan et al. [2022] found that during the campaign, gravity waves with periods smaller than seven hours and greater than two hours were dominated by horizontal structures significantly larger than 500 km. But, it should be noticed that the detailed examination of the waves' activity cannot be performed nor is it the objective of the method described in this work, since we obtain statistical estimates that represent a combination of the divergence(vorticity) that particular structures have.

Extending the analysis to other data sets would also reduce the correlation errors, enabling to test of additional fitting models. For example, the exponent 2/3 can be generalized to an unknown fitting variable (so-called "Hurst parameter"). Preliminary tests applied to the SIMONe 2018 campaign data suggest that the correlations are still too noisy to obtain reliable fitted exponent values. This parameter has been shown to vary for different regions, seasons, and measurement instruments [King et al., 2015a]. In the MLT for example, Roberts and Larsen [2014] were able to reconstruct the second-order structure functions exponent evolution for different stages of turbulence. They used trimethyl aluminum trails from sounding rockets as a tracer of the fluid motions, showing the asymptotic behavior of the parameter as time and horizontal scales increase. In addition, data sets from different SMR network geometries can be helpful to explore either shorter lags, improving zero-lag determinations, or larger lag dynamics, by means of the incorporation of additional terms in equations 21 and 22 to represent an enstrophy cascade origin [Lindborg, 2007], or large-scales planetary waves [Frehlich and Sharman, 2010].

Another important outcome of this work is the estimation of 2D correlation functions of wind fluctuations in the MLT. These functions provide a direct way to characterize the horizontal correlation field from visual inspection and ultimately by statistical analyses. Important properties like the degree of horizontal axisymmetry can be evaluated. This has only been indirectly inferred in the past, for example, with the method by Cho and Lindborg [2001]. The authors compared two types of one-dimensional transverse structure functions, one estimated from theoretical fits (just as we do for the correlations) and the other calculated following the 2D isotropic relation $D'_{TT} = \frac{\mathrm{d}}{\mathrm{d}s_h}\left[s_h D'_{LL}\right]$, where D'_{LL} is the measured longitudinal structure function. From the comparison, they found considerable departures from isotropy in the stratospheric structure functions and lower departures from isotropy in the tropospheric structure functions.

For our case, the degree of horizontal axisymmetry can be inspected in more detail by separating the correlations R'_{uu} and R'_{vv} in different directions, and repeating the Q_{zz} and P estimations for each direction. This method has been applied before by King et al. [2015a], using structure functions in the UTLS. For instance, by separating R'_{uu} and R'_{vv} in Figure 4 between quadrants I and II, it is found that the one-dimensional R'_{LL} component it is well represented by the fitting model in both quadrants, while for the R'_{TT} component, the observations in quadrant II are better represented by the fits than in quadrant I. For both cases $\Psi > \Phi$.

6 Concluding remarks

In this study, it has been demonstrated that the WCFI method has the potential to improve the understanding of the mesoscale dynamics in the MLT. This work analyzes only one of the applications of the method: the estimation of 2D correlation functions and the consequent estimation of longitudinal and transverse correlation functions. As it was shown, this serves to account for the behavior and relative importance of vortical and divergent modes, showing the latter to be more significant in space and wavenumber domain, for the period and location in which the SIMONe 2018 campaign took place. Performing such a comparison in the MLT, using multistatic SMR observations has not been done before.

Exploiting the technique in longer multistatic data sets, measured at different locations such as those provided by SIMONe Argentina [Conte et al., 2021] and SIMONe Perú [Chau et al., 2021] will allow to more efficiently calculate the correlation functions of different spatial and temporal scales and to have a broad view of vortical and divergent modes behavior in the MLT.

Other products of the WCFI technique are temporal correlations, vertical correlations, and horizontal 1D correlation functions, which are currently being explored to characterize other aspects of the upper atmosphere correlation field.

7 Acknowledgments

This work has been supported by the Leibniz SAW project FORMOSA (grant no. K227/2019). The work of J.F.C. is supported by the Bundesministerium für Bildung und Forschung via project WASCLIM-IAP, part of the ROMIC-II program. H. C. A. is supported by DFG under SPP 1788 Dynamic Earth CH1482/2, and by the French Ministry of Foreign and European Affairs for the Eiffel excellence scholarship (File N 945179K).

We thank the Leibniz Institute of Atmospheric Physics personnel T. Barth, N. Gudadze, R. Latteck, N. Pfeffer, M. Clahsen and J. Trautner for supporting the operations of the coded CW links. The data used to generate the figures presented in this paper can be found at: `https://www.radar-service.eu/radar/en/dataset/jcRjcgeflfZOvfSL?token=domLcJVdNGTzAUqTDNNZ` (DOI: 10.22000/536).

A Q_{zz} and P in cartesian ENU system

The derivation of Q_{zz} and P can be performed in cartesian ENU coordinates by expanding equations 3 and 5 as a function of horizontal displacements s_x and s_y. This is achieved by summing over repeated indices, to get

$$Q_{zz} = -\frac{\partial^2 R'_{uu}}{\partial \mathrm{s}_y^2} - \frac{\partial^2 R'_{vv}}{\partial \mathrm{s}_x^2} + 2\frac{\partial^2 R'_{uv}}{\partial \mathrm{s}_y \partial \mathrm{s}_x} \tag{32}$$

$$P = -\frac{\partial^2 R'_{uu}}{\partial \mathrm{s}_x^2} - \frac{\partial^2 R'_{vv}}{\partial \mathrm{s}_y^2} - 2\frac{\partial^2 R'_{uv}}{\partial \mathrm{s}_y \partial \mathrm{s}_x}. \tag{33}$$

It is interesting to note that, $P + Q_{zz} = -\nabla^2 \left(R'_{uu} + R'_{vv}\right)$, which is also valid for R'_{LL} and R'_{TT} when summing P and Q_{zz} from equations 4 and 6, as shown by Lindborg [2007, Eq. 15]. This means that by combining components of the velocity correlation tensor, one might get an idea of the total contribution of vortical and divergent correlation components. In theory, equations 32 and 33 can be used to reproduce the analyses and results developed in this work.

References

V. F. Andrioli, P. P. Batista, B. R. Clemesha, N. J. Schuch, and R. A. Buriti. Multi-year observations of gravity wave momentum fluxes at low and middle latitudes inferred by all-sky meteor radar. *Annales Geophysicae*, 33(9):1183–1193, 2015. doi: 10.5194/angeo-33-1183-2015. URL `https://doi.org/10.5194/angeo-33-1183-2015`.

V. Avsarkisov, E. Becker, and T. Renkwitz. Turbulent parameters in the middle atmosphere: Theoretical estimates deduced from a gravity wave–resolving general circulation model. *Journal of the Atmospheric Sciences*, 79(4):933–952, 2022. doi: 10.1175/JAS-D-21-0005.1.

G. K. Batchelor. *The theory of homogeneous turbulence*. Cambridge university press, 1953.

P. Billant and J.-M. Chomaz. Self-similarity of strongly stratified inviscid flows. *Physics of Fluids*, 13(6):1645–1651, 2001. doi: 10.1063/1.1369125. URL `https://doi.org/10.1063/1.1369125`.

J. Callies, O. Bühler, and R. Ferrari. The dynamics of mesoscale winds in the upper troposphere and lower stratosphere. *Journal of the Atmospheric Sciences*, 73(12):4853 – 4872, 2016. doi: 10.1175/JAS-D-16-0108.1. URL `https://journals.ametsoc.org/view/journals/atsc/73/12/jas-d-16-0108.1.xml`.

H. Charuvil Asokan, J. L. Chau, R. Marino, J. Vierinen, F. Vargas, J. M. Urco, M. Clahsen, and C. Jacobi. Frequency spectra of horizontal winds in the mesosphere and lower thermosphere region from multistatic specular meteor radar observations during the SIMONe 2018 campaign. *Earth, Planets and Space*, 2022. doi: 10.21203/rs.3.rs-697043/v1. URL `https://doi.org/10.21203/rs.3.rs-697043/v1`.

J. L. Chau and M. Clahsen. Empirical phase calibration for multistatic specular meteor radars using a beamforming approach. *Radio Science*, 54(1):60–71, 2019. doi: 10.1029/2018RS006741.

J. L. Chau, G. Stober, C. M. Hall, M. Tsutsumi, F. I. Laskar, and P. Hoffmann. Polar mesospheric horizontal divergence and relative vorticity measurements using multiple specular meteor radars. *Radio Science*, 52(7):811–828, 2017. doi: 10.1002/2016rs006225. URL `https://doi.org/10.1002/2016rs006225`.

J. L. Chau, J. M. Urco, J. P. Vierinen, R. A. Volz, M. Clahsen, N. Pfeffer, and J. Trautner. Novel specular meteor radar systems using coherent MIMO techniques to study the mesosphere and lower thermosphere. *Atmospheric Measurement Techniques*, 12(4):2113–2127, 2019. doi: 10.5194/amt-12-2113-2019. URL `https://doi.org/10.5194/amt-12-2113-2019`.

J. L. Chau, J. M. Urco, J. Vierinen, B. J. Harding, M. Clahsen, N. Pfeffer, K. M. Kuyeng, M. A. Milla, and P. J. Erickson. Multistatic specular meteor radar network in peru: System description and initial results. *Earth and Space Science*, 8(1), 2021. doi: 10.1029/2020ea001293. URL `https://doi.org/10.1029/2020ea001293`.

J. Y. N. Cho and E. Lindborg. Horizontal velocity structure functions in the upper troposphere and lower stratosphere: 1. observations. *Journal of Geophysical Research: Atmospheres*, 106(D10):10223–10232, 2001. doi: 10.1029/2000jd900814. URL `https://doi.org/10.1029/2000jd900814`.

B. R. Clemesha, P. P. Batista, R. A. B. da Costa, and N. Schuch. Seasonal variations in gravity wave activity at three locations in brazil. *Annales Geophysicae*, 27(3):1059–1065, 2009. doi: 10.5194/angeo-27-1059-2009. URL `https://doi.org/10.5194/angeo-27-1059-2009`.

J. F. Conte, J. L. Chau, J. M. Urco, R. Latteck, J. Vierinen, and J. O. Salvador. First studies of mesosphere and lower thermosphere dynamics using a multistatic specular meteor radar network over southern patagonia. *Earth and Space Science*, 8(2), 2021. doi: 10.1029/2020ea001356. URL `https://doi.org/10.1029/2020ea001356`.

P. J. Espy, G. O. L. Jones, G. R. Swenson, J. Tang, and M. J. Taylor. Seasonal variations of the gravity wave momentum flux in the antarctic mesosphere and lower thermosphere. *Journal of Geophysical Research: Atmospheres*, 109 (D23):1–9, 2004. doi: https://doi.org/10.1029/2003JD004446.

R. Frehlich and R. Sharman. Climatology of velocity and temperature turbulence statistics determined from rawinsonde and ACARS/AMDAR data. *Journal of Applied Meteorology and Climatology*, 49(6):1149–1169, 2010. doi: 10.1175/2010jamc2196.1. URL `https://doi.org/10.1175/2010jamc2196.1`.

U. Frisch. Why a probabilistic description of turbulence? In *Turbulence. The Legacy of A. N. Kolmogorov*, pages 27–39. Cambridge University Press, 1995. doi: 10.1017/cbo9781139170666.004. URL `https://doi.org/10.1017/cbo9781139170666.004`.

K. Hamilton, Y. O. Takahashi, and W. Ohfuchi. Mesoscale spectrum of atmospheric motions investigated in a very fine resolution global general circulation model. *Journal of Geophysical Research: Atmospheres*, 113(D18), 2008. doi: 10.1029/2008jd009785. URL `https://doi.org/10.1029/2008jd009785`.

C. O. Hines. A modeling of atmospheric gravity waves and wave drag generated by isotropic and anisotropic terrain. *Journal of the Atmospheric Sciences*, 45 (2):309–322, 1988. doi: 10.1175/1520-0469(1988)045⟨0309:amoagw⟩2.0.co;2. URL `https://doi.org/10.1175/1520-0469(1988)045<0309:amoagw>2.0.co;2`.

W. Hocking, B. Fuller, and B. Vandepeer. Real-time determination of meteor-related parameters utilizing modern digital technology. *Journal of Atmospheric and Solar-Terrestrial Physics*, 63(2-3):155–169, 2001. doi: 10.1016/s1364-6826(00)00138-3. URL `https://doi.org/10.1016/s1364-6826(00)00138-3`.

P. Hoffmann, E. Becker, W. Singer, and M. Placke. Seasonal variation of mesospheric waves at northern middle and high latitudes. *Journal of Atmospheric and Solar-Terrestrial Physics*, 72(14-15):1068–1079, 2010. doi: 10.1016/j.jastp.2010.07.002. URL `https://doi.org/10.1016/j.jastp.2010.07.002`.

D. A. Holdsworth, I. M. Reid, and M. A. Cervera. Buckland park all-sky interferometric meteor radar. *Radio Science*, 39(5):n/a–n/a, 2004. doi: 10.1029/2003rs003014. URL `https://doi.org/10.1029/2003rs003014`.

C. Jacobi, Y. Portnyagin, T. Solovjova, P. Hoffmann, W. Singer, A. Fahrutdinova, R. Ishmuratov, A. Beard, N. Mitchell, H. Muller, R. Schminder, D. Kürschner, A. Manson, and C. Meek. Climatology of the semidiurnal tide at 52-56° n from ground-based radar wind measurements 1985–1995. *Journal of Atmospheric and Solar-Terrestrial Physics*, 61(13):975–991, 1999. doi: 10.1016/s1364-6826(99)00065-6. URL https://doi.org/10.1016/s1364-6826(99)00065-6.

G. P. King, J. Vogelzang, and A. Stoffelen. Second-order structure function analysis of scatterometer winds over the tropical pacific. *Journal of Geophysical Research: Oceans*, 120(1):362–383, 2015a. doi: 10.1002/2014jc009992. URL https://doi.org/10.1002/2014jc009992.

G. P. King, J. Vogelzang, and A. Stoffelen. Upscale and downscale energy transfer over the tropical pacific revealed by scatterometer winds. *Journal of Geophysical Research: Oceans*, 120(1):346–361, 2015b. doi: 10.1002/2014jc009993. URL https://doi.org/10.1002/2014jc009993.

A. N. Kolmogorov. The local structure of turbulence in incompressible viscous fluid for very large reynolds numbers. *Doklady Akademii Nauk SSSR*, 30:301–305, 1941.

E. Lindborg. Can the atmospheric kinetic energy spectrum be explained by two-dimensional turbulence? *Journal of Fluid Mechanics*, 388:259–288, 1999. doi: 10.1017/S0022112099004851.

E. Lindborg. The energy cascade in a strongly stratified fluid. *Journal of Fluid Mechanics*, 550(-1):207, Feb. 2006. doi: 10.1017/s0022112005008128. URL https://doi.org/10.1017/s0022112005008128.

E. Lindborg. Horizontal wavenumber spectra of vertical vorticity and horizontal divergence in the upper troposphere and lower stratosphere. *Journal of the Atmospheric Sciences*, 64(3):1017–1025, 2007. doi: 10.1175/jas3864.1. URL https://doi.org/10.1175/jas3864.1.

E. Lindborg. A helmholtz decomposition of structure functions and spectra calculated from aircraft data. *Journal of Fluid Mechanics*, 762, 2014. doi: 10.1017/jfm.2014.685. URL https://doi.org/10.1017/jfm.2014.685.

A. Marenco, V. Thouret, P. Nédélec, H. Smit, M. Helten, D. Kley, F. Karcher, P. Simon, K. S. Law, J. A. Pyle, G. Poschmann, R. V. Wrede, C. J. Hume, and T. Cook. Measurement of ozone and water vapor by airbus in-service aircraft: The mozaic airborne program, an overview. *Journal of Geophysical Research*, 103:25631–25642, 1998.

J. P. McCormack, L. Coy, and W. Singer. Intraseasonal and interannual variability of the quasi 2 day wave in the northern hemisphere summer mesosphere. *Journal of Geophysical Research: Atmospheres*, 119(6):2928–2946, 2014. doi: 10.1002/2013jd020199. URL https://doi.org/10.1002/2013jd020199.

J. C. McDowell. The edge of space: Revisiting the karman line. *Acta Astronautica*, 151:668–677, 2018. doi: 10.1016/j.actaastro.2018.07.003. URL `https://doi.org/10.1016/j.actaastro.2018.07.003`.

G. D. Nastrom, K. S. Gage, and W. H. Jasperson. Kinetic energy spectrum of large-and mesoscale atmospheric processes. *Nature*, 310(5972):36–38, 1984. doi: 10.1038/310036a0. URL `https://doi.org/10.1038/310036a0`.

M. J. Nicolls, D. C. Fritts, D. Janches, and C. J. Heinselman. Momentum flux determination using the multi-beam poker flat incoherent scatter radar. *Annales Geophysicae*, 30(6):945–962, 2012. doi: 10.5194/angeo-30-945-2012. URL `https://doi.org/10.5194/angeo-30-945-2012`.

M. Placke, P. Hoffmann, E. Becker, C. Jacobi, W. Singer, and M. Rapp. Gravity wave momentum fluxes in the MLT—part II: Meteor radar investigations at high and midlatitudes in comparison with modeling studies. *Journal of Atmospheric and Solar-Terrestrial Physics*, 73(9):911–920, 2011. doi: 10.1016/j.jastp.2010.05.007. URL `https://doi.org/10.1016/j.jastp.2010.05.007`.

B. Roberts and M. Larsen. Structure function analysis of chemical tracer trails in the mesosphere-lower thermosphere region. *Journal of Geophysical Research: Atmospheres*, 119(11):6368–6375, 2014. doi: 10.1002/2013jd020796. URL `https://doi.org/10.1002/2013jd020796`.

C.-G. Rossby. Relation between variations in the intensity of the zonal circulation of the atmosphere and the displacements of the semipermanent centers of action. *Journal of Marine Research*, 2:38–55, 1939.

D. J. Sandford, H. G. Muller, and N. J. Mitchell. Observations of lunar tides in the mesosphere and lower thermosphere at arctic and middle latitudes. *Atmospheric Chemistry and Physics*, 6(12):4117–4127, 2006. doi: 10.5194/acp-6-4117-2006. URL `https://doi.org/10.5194/acp-6-4117-2006`.

E. O. Schulz-DuBois and I. Rehberg. Structure function in lieu of correlation function. *Applied Physics A*, 24(4):323–329, 1981. doi: 10.1007/bf00899730. URL `https://doi.org/10.1007/bf00899730`.

W. C. Skamarock, S.-H. Park, J. B. Klemp, and C. Snyder. Atmospheric kinetic energy spectra from global high-resolution nonhydrostatic simulations. *Journal of the Atmospheric Sciences*, 71(11):4369–4381, 2014. doi: 10.1175/jas-d-14-0114.1. URL `https://doi.org/10.1175/jas-d-14-0114.1`.

G. Stober and J. L. Chau. A multistatic and multifrequency novel approach for specular meteor radars to improve wind measurements in the MLT region. *Radio Science*, 50(5):431–442, 2015. doi: 10.1002/2014rs005591. URL `https://doi.org/10.1002/2014rs005591`.

J. M. Urco, J. L. Chau, M. A. Milla, J. P. Vierinen, and T. Weber. Coherent MIMO to improve aperture synthesis radar imaging of field-aligned irregularities: First results at jicamarca. *IEEE Transactions on Geoscience and Remote Sensing*, 56(5):2980–2990, 2018. doi: 10.1109/tgrs.2017.2788425. URL `https://doi.org/10.1109/tgrs.2017.2788425`.

J. M. Urco, J. L. Chau, T. Weber, and R. Latteck. Enhancing the spatiotemporal features of polar mesosphere summer echoes using coherent MIMO and radar imaging at MAARSY. *Atmospheric Measurement Techniques*, 12(2):955–969, 2019. doi: 10.5194/amt-12-955-2019. URL `https://doi.org/10.5194/amt-12-955-2019`.

F. Vargas, J. L. Chau, H. C. Asokan, and M. Gerding. Mesospheric gravity wave activity estimated via airglow imagery, multistatic meteor radar, and SABER data taken during the SIMONe–2018 campaign. *Atmospheric Chemistry and Physics*, 21(17):13631–13654, 2021. doi: 10.5194/acp-21-13631-2021. URL `https://doi.org/10.5194/acp-21-13631-2021`.

J. Vierinen, J. L. Chau, N. Pfeffer, M. Clahsen, and G. Stober. Coded continuous wave meteor radar. *Atmospheric Measurement Techniques*, 9(2):829–839, 2016. doi: 10.5194/amt-9-829-2016. URL `https://doi.org/10.5194/amt-9-829-2016`.

J. Vierinen, J. L. Chau, H. Charuvil, J. M. Urco, M. Clahsen, V. Avsarkisov, R. Marino, and R. Volz. Observing mesospheric turbulence with specular meteor radars: A novel method for estimating second-order statistics of wind velocity. *Earth and Space Science*, 6(7):1171–1195, 2019. doi: 10.1029/2019ea000570. URL `https://doi.org/10.1029/2019ea000570`.

R. Volz, J. L. Chau, P. J. Erickson, J. P. Vierinen, J. M. Urco, and M. Clahsen. Four-dimensional mesospheric and lower thermospheric wind fields using gaussian process regression on multistatic specular meteor radar observations. *Atmospheric Measurement Techniques*, 2021. doi: 10.5194/amt-2021-40. URL `https://doi.org/10.5194/amt-2021-40`.

J. Xu, H.-L. Liu, W. Yuan, A. K. Smith, R. G. Roble, C. J. Mertens, J. M. Russell, and M. G. Mlynczak. Mesopause structure from thermosphere, ionosphere, mesosphere, energetics, and dynamics (TIMED)/sounding of the atmosphere using broadband emission radiometry (SABER) observations. *Journal of Geophysical Research*, 112(D9), 2007. doi: 10.1029/2006jd007711. URL `https://doi.org/10.1029/2006jd007711`.

J. P. Younger and I. M. Reid. Interferometer angle-of-arrival determination using precalculated phases. *Radio Science*, 52(9):1058–1066, 2017. doi: 10.1002/2017RS006284.

W. Zhong, X. Xue, W. Yi, I. M. Reid, T. Chen, and X. Dou. Error analyses of a multistatic meteor radar system to obtain a three-dimensional spatial-resolution distribution. *Atmospheric Measurement Techniques*, 14(5):3973–

3988, 2021. doi: 10.5194/amt-14-3973-2021. URL https://doi.org/10.5194/amt-14-3973-2021.